

HI scaling relations of galaxies in the environment of HI-rich and control galaxies observed by the Bluedisk project

Enci Wang^{1*}, Jing Wang^{2,3}, Guinevere Kauffmann², Gyula I. G. Józsa^{4,5,6},
Cheng Li¹

¹*Partner Group of the Max Planck Institute for Astrophysics at the Shanghai Astronomical Observatory and Key Laboratory for Research in Galaxies and Cosmology of Chinese Academy of Sciences, Nandan Road 80, Shanghai 200030, China*

²*Max-Planck-Institut für Astrophysik, Karl-Schwarzschild-Str. 1, D-85741 Garching, Germany*

³*CSIRO Astronomy and Space Science, Australia Telescope National Facility, PO Box 76, Epping, NSW 1710, Australia*

⁴*SKA South Africa, Radio Astronomy Research Group, 3rd Floor, The Park, Park Road, Pinelands, 7405, South Africa*

⁵*Rhodes University, Department of Physics and Electronics, Rhodes Centre for Radio Astronomy Techniques and Technologies, PO Box 94, Grahamstown, 6140, South Africa*

⁶*Argelander-Institut für Astronomie, Auf dem Hügel 71, 53121 Bonn, Germany*

Accepted Received; in original form

ABSTRACT

Our work is based on the “Bluedisk” project, a program to map the neutral gas in a sample of 25 HI-rich spirals and a similar number of control galaxies with the Westerbork Synthesis Radio Telescope (WSRT). In this paper we focus on the HI properties of the galaxies in the environment of our targeted galaxies. In total, we extract 65 galaxies from the WSRT cubes with stellar masses between $10^8 M_\odot$ and $10^{11} M_\odot$. Most of these galaxies are located on the same HI mass-size relation and “HI-plane” as normal spiral galaxies. We find that companions around HI-rich galaxies tend to be HI-rich as well and to have larger $R_{90, \text{HI}}/R_{50, \text{HI}}$. This suggests a scenario of “HI conformity”, similar to the colour conformity found by Weinmann et al. (2006): galaxies tend to adopt the HI properties of their neighbours. We visually inspect the outliers from the HI mass-size relation and galaxies which are offset from the HI plane and find that they show morphological and kinematical signatures of recent interactions with their environment. We speculate that these outliers have been disturbed by tidal or ram-pressure stripping processes, or in a few cases, by accretion events.

Key words: atomic gas; HI mass-size relation; HI-plane; cold gas accretion; tidal/ram pressure stripping

1 INTRODUCTION

In the recent years, a large number of surveys have obtained multi-wavelength imaging and spectroscopy for large samples of galaxies at different redshifts. Thanks to these surveys, we have learned a lot about how galaxies form and evolve. However, many physical processes, such as the regulation of star formation by gas accretion, remain poorly understood.

The accretion of cold gas in the form of gas-rich dwarf galaxies can bring gas to galaxies and fuel star formation (Sancisi et al. 2008; Silk & Mamon 2012; Conselice et al. 2013). The presence of extra-planar gas (Chaves & Irwin

2001; Boomsma et al. 2005; Wakker et al. 2007), lopsided HI morphologies (Sancisi 1976; Shang et al. 1998; Thilker et al. 2007) and gas tails (Kregel & Sancisi 2001; Oosterloo et al. 2010) may directly be linked to ongoing cold gas accretion through mergers. While some portion of the gas in galaxies is being acquired through the accretion of dwarf galaxies, the inferred gas accretion rate is not sufficient to sustain star formation in galaxies ($\sim 1.0 M_\odot \text{ yr}^{-1}$) (Binney, Dehnen & Bertelli 2000). As a consequence, a large fraction of gas should be accreted directly from the Inter-galactic Medium (IGM). Low-density galaxies lose their gas through tidal interactions or ram pressure stripping, which may finally quench their star formation (Moore et al. 1996; Calcáneo-Roldán et al. 2000; Mayer et al. 2006; McCarthy et al. 2008; Kapferer et al. 2008; Chang, Macciò & Kang

* E-mail: ecwang@shao.ac.cn

2013). This process happens more frequently in dense environments.

The Bluedisk project, which was carried out with the Westerbork Synthesis Radio Telescope (WSRT), was designed to map the HI distribution in a sample of 25 unusually HI-rich galaxies. Galaxies with large HI excess usually have bluer and younger outer disks (Wang et al. 2011), and more metal-poor ionized gas (Moran et al. 2012). A sample of 25 control galaxies was also observed for comparison. These galaxies were closely matched in stellar mass, stellar surface mass density, redshift and inclination, but were not unusually rich in HI. The goal of the project was to determine whether there was any evidence for recent gas accretion onto unusually HI-rich galaxies by investigating and contrasting the HI structure and environment of the gas-rich galaxies with that of the control sample.

In the first paper of Bluedisk project, Wang et al. (2013, Paper I) concentrated on the HI size and morphology of the 42 targeted galaxies. They found that HI-rich galaxies do not differ from normal galaxies with respect to HI asymmetry indices or optical/HI disk position angle differences. This is inconsistent with a scenario in which the excess gas was brought in by mergers. In this paper, we extend this work to the galaxies in the neighbourhood of the targeted galaxies that lie within the WSRT data cubes.

Our paper is organized as follows. In section 2, we briefly recap our observations, describe the data and the data processing that we carried out for our environmental study, including our procedure for accurate primary beam correction. In section 3, we discuss our identification of galaxy neighbours via cross-matching with the spectroscopic catalogue of the Sloan Digital Sky Survey (SDSS) and how we build a uniform catalog of these sources. In section 4, we examine the HI mass-size relation and the correlation between HI and optical properties such as mass and stellar surface density for both the neighbours around HI-rich and control galaxies. In section 5, we discuss the morphology and properties of galaxies which are found to be outliers from the standard scaling relations. We summarize our results in section 6.

Throughout this paper, all the distance-dependent parameters are computed with $\Omega = 0.3$, $\Lambda = 0.7$ and $H_0 = 70$ km s⁻¹ Mpc⁻¹.

2 DATA

2.1 Observation and data reduction

The 50 targets were observed with the WSRT in 2011 and 2012. Target selection and data reduction are described in detail in Paper I. For detailed information on the targeted galaxies we refer the reader to table 1 in Paper I.

The HI raw data cubes were reduced using a pipeline produced by Serra et al. (2012), based on the Miriad reduction package (Sault, Teuben & Wright 1995). The data used in this paper are HI cubes built with a Robust weighting of 0.4, which provides a suitable compromise between sensitivity and resolution. The pixel size is 4 arcsec and the velocity width for each channel is about 13 km s⁻¹. The velocity resolution is 26 km s⁻¹ (FWHM). The typical beam has Half-Power Beamwidth (HPBW) of $16 \times 16/\sin(\delta)$ arcsec², where δ is the declination. Every cube has 148 channels,

covers a redshift range of $\Delta z = 0.006$, and has a size of 1 degree on each side, which corresponds to a physical scale of 1.7 Mpc at a redshift $z = 0.025$. We point out that 92.0% of the galaxies are within a systematic velocity difference of 500 km s⁻¹ from the primary galaxies. However, some untargeted galaxies are not in the immediate neighborhood of the primary galaxies: in the radial direction, the farthest galaxy is 884 km s⁻¹ away. Hence we are investigating a relatively large-scale environmental effect rather than the direct interaction between galaxy pairs in this paper.

We generate two-dimensional HI total-intensity maps (moment-0 maps) for each cube. First we identify 3-d regions of emission by a smoothing and clipping algorithm. We then add all the detected HI emission from all velocity channels. We also estimate errors for all non-zero pixels in the HI intensity map.

2.2 Physical properties of galaxies

The physical quantities required for this work are a spectrophotometric estimate of the stellar mass M_* , stellar surface mass density μ_* , and the NUV-r colour. Stellar masses were taken from the MPA-JHU database (<http://www.mpa-garching.mpg.de/SDSS/DR7/>), and are derived from Sloan Digital Sky Survey (SDSS) photometry. The stellar surface mass density is defined as $\mu_* = M_*/(2\pi R_{50,z}^2)$, where $R_{50,z}$ is the physical radius which contains half the total light in the z-band. The NUV magnitude is available from the Galaxy Evolution Explorer (GALEX) pipeline and the NUV-r colors are corrected for Galactic extinction. The HI size $R1$, $R_{50,\text{HI}}$, $R_{90,\text{HI}}$ and rs , and HI mass M_{HI} , are measured using our HI data cubes. $R1$ is the radius where radially averaged face-on HI column density reaches $1 \text{ M}_\odot \text{ pc}^{-2}$ (corresponding to $1.25 \times 10^{20} \text{ atoms cm}^{-2}$). $R_{50,\text{HI}}$ and $R_{90,\text{HI}}$ are the radii enclosing 50 and 90 percent of the HI flux, respectively. Note that an inclination correction is not applied when calculating $R1$ for unresolved galaxies ($R_{50,\text{HI}}$ less than 15 arcsec), because their HI sizes are less than the beam size. For these galaxies, the derived value of $R1$ should be regarded as an upper limit to the true value of $R1$. rs is the scale-length of the outer exponential disk, and is measured by assuming a PSF-convolved two-component model for the radial distribution of HI (see Wang et al. 2014 for details). The HI mass is defined as $M_{\text{HI}} = 2.356 \times 10^5 (D_{\text{lum}} \text{ Mpc}^{-1})^2 (F_{\text{tot}} \text{ Jy km s}^{-1})^{-1}$, where D_{lum} is the luminosity distance and F_{tot} is the integrated HI-line flux density. The measurements of these parameters are described in more detail in Paper I.

2.3 Primary beam correction

Our work depends critically on the primary beam correction, which accounts for the attenuation by the primary beam towards large radii. We consider two methods. One is a non-parametric model (data cube) provided by Popping & Braun (2008), the other one is to apply a parametric correction function of the form $\cos^6(c \times \nu \times d)$ as routinely used for the WSRT, where ν is the frequency in GHz, and d is the angular distance from the pointing centers in degrees.

To test and calibrate both approaches, we compare the un-corrected flux densities of point sources in the radio continuum maps, which are an additional product of our data

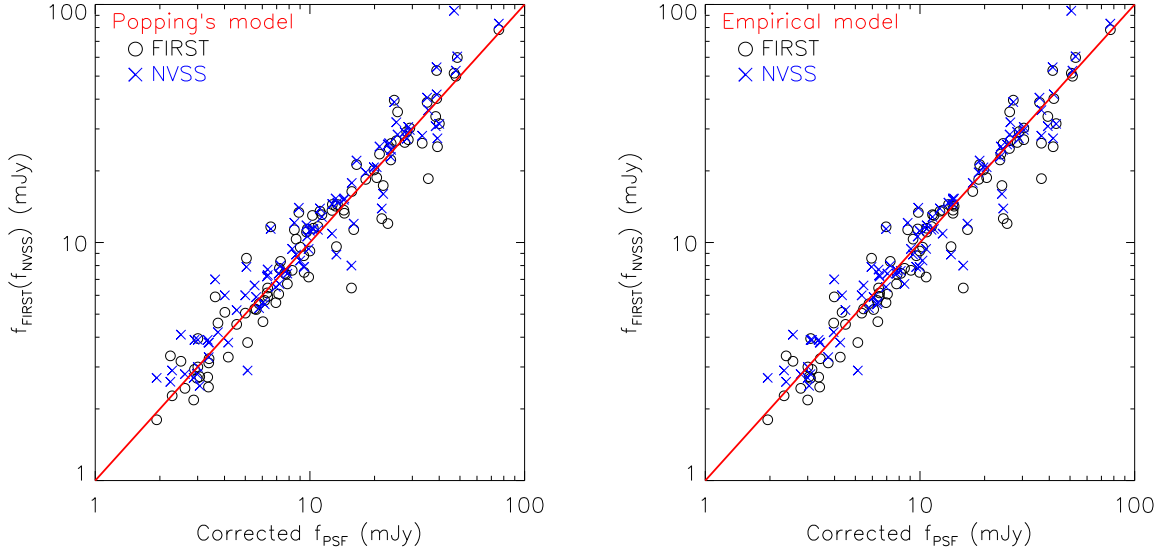


Figure 1. Test of the two methods for primary beam correction: 1) applying the standard WSRT analytic model (with $c=63$), and 2) a nonparametric model by Popping & Braun (2008). This figure shows the relation between the primary beam corrected flux density and the FIRST/NVSS flux density. Black circles and blue crosses represent the FIRST data and the NVSS data, respectively. The left and right panels are for Popping’s model and the empirical model, respectively.

reduction pipeline (see Wang et al. 2013) with the flux densities listed in the NRAO FIRST (Becker, White & Helfand 1995, Faint Images of the Radio Sky at Twenty-Centimeters) and NVSS (Condon et al. 1998, NRAO VLA Sky Survey) catalogues.

Specifically, we first extract sources from our continuum maps using Source Extractor (SE). Then we use the point spread function (PSF) fitting method to derive the flux density of each source extracted from our continuum maps. With a detection threshold of 5σ , where σ is the rms noise with a typical value of 8.0×10^{-5} Jy beam $^{-1}$, we extract more than two thousand sources from all images. This catalog is then matched to the FIRST and NVSS catalogs. In total, there are 4128 sources in the FIRST catalog (Becker et al. 2012, 12Feb16 Version) located in these 50 HI observed regions, with integral flux density greater than 1 mJy. Among them, 1322 sources are classified as point sources at FIRST resolution (with a major axis FWHM of 2 arcsec). About one hundred detections in our cubes were matched with both FIRST and NVSS point sources. We restrict the analysis to point sources because FIRST and NVSS flux densities are very consistent with each other for point sources, with a scatter of 0.05 dex.

This way, we obtain an best-fit c of 63, differing distinctly from the commonly used and recommended $c = 68$ (see WSRT web pages). This difference in c causes a 0.46 dex difference in flux intensity for pixels at the farthest edge of the continuum map (0.71 degree from the map center at redshift $z = 0.025$), and a largest difference of 0.17 dex for our farthest detected source. On average, the flux densities corrected with $c = 63$ are 0.04 dex smaller than that of $c = 68$ for our untargeted sources. Fig. 1 shows the comparison between the primary beam corrected PSF flux densities from our continuum maps and the FIRST/NVSS flux densities using both methods, the empirical analytic (standard)

model, and Popping’s nonparametric model. We can see a good linear correlation between the corrected PSF flux density and the FIRST/NVSS data. It is difficult to tell which model is better according to the data points, because the scatter is similar (~ 0.7 dex). However, we remark that the standard recommended analytic model with $c = 68$ would have provided an insufficient primary beam correction in the wavelength range considered in this work. Since we confirm that the model of Popping & Braun (2008) works well, we adopt it for our primary beam correction for the Bluedisk data cubes.

3 SOURCE IDENTIFICATION

We use the source finder developed by Serra et al. (2012) to detect sources in the cubes. The pipeline uses a smooth-and-clip algorithm: it smooths the cube and searches for regions with a flux intensity above 3σ of the cube. The resulted catalog of 1962 sources includes both real sources and noise peaks. We take a few steps to filter the real galaxies with reliable flux measurements. The first step is to match the HI catalog with the SDSS spectroscopic catalog. 163 HI sources are matched with optical galaxies, with an angular distance smaller than 20 arcsec (roughly the beam size). 10 of them have more than one matched optical counterpart. We further constrain in redshift by requiring $|z_{\text{spec}} - z_{\text{HI}}| < 0.001$, which left us with 120 HI sources, and none of them have multiple optical counterparts. Although we may miss the galaxies with no optical spectroscopic observation, we efficiently exclude most of the unreliable sources from the HI catalog.

In the following sections, we describe how we further select the sources with reliable HI flux measurements.

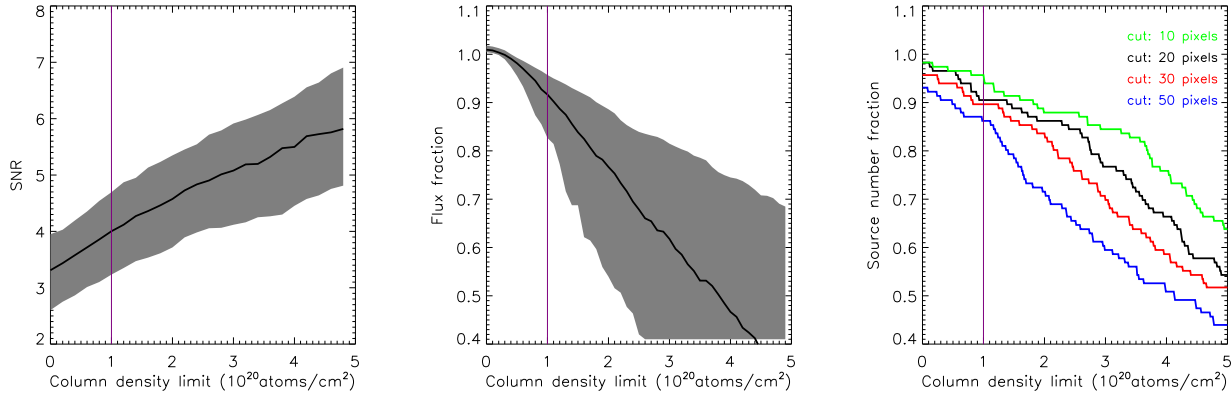


Figure 2. The left panel shows the SNR varies with applying different column density limits. The middle panel shows the flux fraction varies with increasing column density limit. The flux fraction is the ratio of the total HI flux above a specific column density limit to the HI flux without giving a column density limit. The right panel shows the column density limit versus the fraction of retained sources. The color curves represent different pixel number cuts (If the effective pixel number of the source is greater than the cut, it is treated as a source).

3.1 Defining the outermost HI contour

In Paper I, we describe how we build error maps for the HI moment-0 images. We use these error maps to determine a HI column density threshold that reliably defines an outermost contour for morphological analysis. The outermost contour should also contain most of the total flux of the source. The left panel of Fig. 2 shows the signal-to-noise ratio at different HI column density levels for all the detected sources. The black curve shows the median signal-to-noise ratio, and the gray region shows the 20% to 80% percentile range. The SNR is typically above 3 when the threshold is set to be 10^{20} atoms cm⁻².

The middle panel of Fig. 2 shows how the fraction of the total flux of the galaxy varies as a function of column density limit. The black curve shows the median flux fraction for all sources, and the gray region shows the 20% to 80% percentile range.¹ We see that most of the galaxies retain more than 90% of their total flux when the limiting contour level is 10^{20} atoms cm⁻².

We require sources to contain at least 20 pixels in the moment-0 maps to be included in our catalogues. In the right panel of Fig. 2, we show the fraction of sources that meet this criterion as a function of different density threshold cuts (the black curve). We also show how the curve changes if we change the resolving criteria to 10, 30 and 40 pixels. We can see more than 90% of the sources are resolved with 20 pixels at a density detection threshold of 10^{20} atoms cm⁻².

Based on the analysis shown above, we adopt 10^{20} atoms cm⁻² as our HI column density threshold, because it is demonstrated to be a good threshold for reliably describing the shape and size of the HI while still retaining most of the HI mass, and it also includes most of the well-resolved HI sources.

¹ At a column density limit of zero, the HI flux fraction is larger than 1.0 for all galaxies, because by clipping at that level, the noise contribution is neglected (i.e., some negative total flux from negative noise peaks has to be added to counterweight this effect at the edges of the detected sources).

3.2 Extracting sources with reliable HI fluxes

To estimate the reliability of our determinations of the total HI flux, we use a bootstrap method. We simulate a set of repeat observations by adding random noise with the same characteristics as the noise in the Bluedisk cubes, and measure the resulting variance if the total HI flux. In practice, we take the channels that have no detected sources from the data cube, and randomly repeat them to make noise cubes that have the same size as the Bluedisk data cubes. We add the noise cubes to the original Bluedisk cubes to make a “perturbed” cube. We repeat this process 10 times for each original Bluedisk cube. In addition, we also generate error maps for these simulated cubes.

The left panel of Fig. 3 shows how the scatter in the derived HI between the different perturbed cubes varies function of the original fluxes. The HI flux scatter rises sharply for HI fluxes less than 0.5 Jy km s^{-1} , and becomes almost flat at a value of about 0.04 dex for HI fluxes greater than 0.5 Jy km s^{-1} .

The right panel of Fig. 3 shows the distribution of the ratios of simulated HI fluxes and input HI fluxes in two flux bins. The black histogram shows the ratio of the distribution for galaxies with HI fluxes greater than 0.5 Jy km s^{-1} , and the red dot-and-dash histogram shows the distribution for galaxies with HI fluxes less than 0.5 Jy km s^{-1} . The simulated HI fluxes in the lower HI flux bin are clearly more scattered than in the higher HI flux bin. We further select galaxies that have a SNR of at least 3 for the 10^{20} atoms cm⁻² HI column density contour. The distribution of their flux ratios is shown as the red histogram in Fig. 3. We find it to be similar to that of galaxies with high HI flux. In what follows, we exclude low HI flux sources (total HI fluxes less than 0.5 Jy km s^{-1}) with a SNR of less than 3 in the 10^{20} atoms cm⁻² contour. Our tests show that this ensures that the error in the HI fluxes we measured will be less than about 0.04 dex.

There are 43 targeted galaxies and 65 additional galaxies in the final sample. Among the galaxies that were not targeted, 45 galaxies are resolved and 20 galaxies are un-

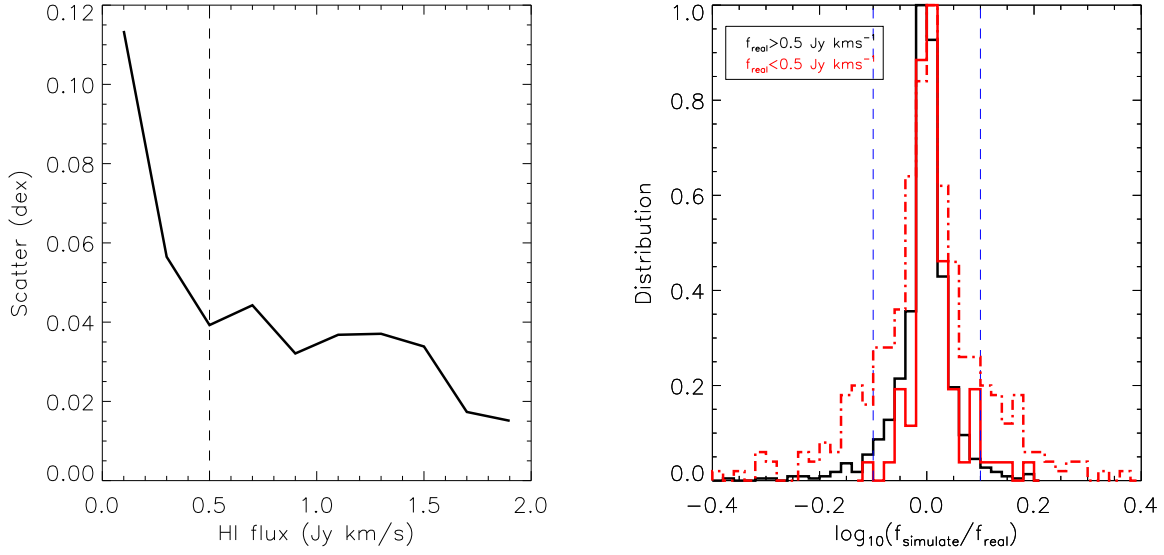


Figure 3. The left panel shows the changing of HI flux scatter with different HI flux bins for simulated sources. The right panel shows the distributions of HI flux ratio for HI flux intervals for simulated sources. The black histogram represents the distribution of HI flux ratio for HI flux greater than 0.5 Jy km s^{-1} , and the red dot-and-dash histogram is for galaxies with HI flux less than 0.5 Jy km s^{-1} . Besides, the red histogram is also for galaxies with HI flux less than 0.5 Jy km s^{-1} , but with SNR greater than 3.

resolved. Among these additional galaxies, 15 galaxies are located in the “peculiar cubes” (Wang et al. 2013), in which the targeted galaxy is not detected in HI or is otherwise disturbed. We exclude these galaxies in the analysis described below. We also divide our targeted galaxies into two parts according to whether they lie above or below the HI-plane defined in Catinella et al. (2010). Hereafter, targeted galaxies which lie above the HI-plane are referred to HI-rich galaxies (blue sample) and the cubes they reside in are referred as blue cubes. Similarly, the rest of targeted galaxies are referred as control sample and the rest of cubes are referred as control cubes. This definition is different to what was designed in observation, but it properly reflects the actual HI content of each system. At last, 23 blue targeted galaxies, 20 control targeted galaxies, 26 untargeted galaxies in blue cubes and 24 untargeted galaxies in control cubes are left.

The detailed properties of all the additional detected galaxies are listed in table 1. Galaxies in “peculiar cubes” are also listed in this table, but not used for analysis in the following part of the paper. As can be seen, they span stellar masses from $10^8 - 10^{11} M_{\odot}$ and HI masses from $10^{8.5} - 10^{10.4} M_{\odot}$. Although our sample is small in size, it is unique in that it samples the environments rare, very HI-rich systems. Most of the galaxies are resolved in HI, enabling us to study their resolved morphology and their kinematics. Compared to the Westerbork observations of neutral Hydrogen in Irregular and SPiral galaxies (WHISP), our data are more sensitive.

4 RESULTS

The mass distribution for our final sample is shown in Fig. 4. The sample is divided into four subsamples: the blue tar-

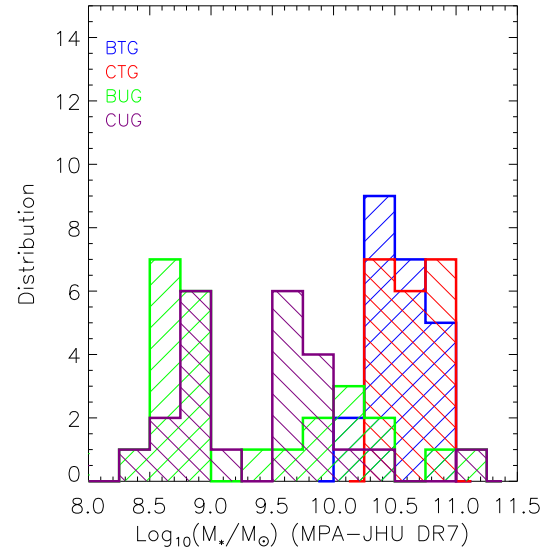


Figure 4. Stellar mass distribution of our sample. The stellar mass is from the MPA-JHU DR7 catalogue. Our sample is divided into BTG (blue), CTG (red), BUG (green) and CUG (purple).

geted galaxies (BTG), the control targeted galaxies (CTG), the additional galaxies located in blue cubes (BUG) and the additional galaxies located in control cubes (CUG). By selection, all targeted galaxies are massive with $\log M_*/M_{\odot} > 10$. The additional galaxies have a very broad stellar mass distribution from $10^8 M_{\odot}$ to $10^{11} M_{\odot}$. The goal of this paper is to study their HI properties.

ID	ra	dec	z	$\log M_*$ M_\odot	μ_* $M_\odot \text{kpc}^{-2}$	NUV-r	$\log M_{\text{HI}}$ M_\odot	<i>Dis</i> degree	<i>R1</i> arcsec	$R_{50,\text{HI}}$ arcsec	$R_{90,\text{HI}}$ arcsec	<i>rs</i> arcsec
14	112.31934	42.27963	0.02307	10.39	8.33	2.87	9.88	0.30	61	31	57	3.8
78	123.48852	52.64847	0.01820	11.01	8.99	3.80	10.40	0.22	140	63	132	16.4
84	123.03966	52.45524	0.01874	9.61	8.14	2.03	9.55	0.16	46	23	41	-
143	127.30350	40.85448	0.02510	9.33	7.74	2.49	8.77	0.21	16	12	21	37.0
179	127.73492	55.83517	0.02542	8.91	7.53	2.56	8.73	0.39	15	11	21	6.1
221	129.17748	41.47231	0.02919	9.88	8.29	1.94	9.80	0.08	42	24	46	11.9
248	129.80326	30.92383	0.02569	8.51	7.10	2.03	9.19	0.19	23	17	31	15.4
306	132.05204	36.78074	0.02527	10.24	8.49	2.52	9.46	0.24	32	16	29	4.1
307	132.66660	36.46876	0.02521	6.98	6.98	1.51	9.94	0.35	57	25	55	-
346	132.02870	41.85922	0.02997	10.11	7.99	2.64	9.53	0.26	32	21	36	-
370	137.21930	44.93228	0.02657	10.27	9.31	3.62	8.96	0.13	14	14	43	7.9
375	137.33753	45.03975	0.02730	8.89	7.25	1.63	9.55	0.26	37	17	31	7.3
394	138.20927	40.49874	0.02759	9.60	8.03	2.17	9.73	0.41	37	18	37	7.4
396	138.39333	40.46574	0.02758	8.59	7.12	1.93	9.34	0.35	27	16	26	4.8
444	138.37436	51.31519	0.02773	8.80	7.25	-	9.33	0.23	25	13	27	28.8
446	138.53751	51.41797	0.02805	9.51	8.59	-	9.17	0.14	21	14	32	8.7
454	138.84323	51.05039	0.02881	9.68	7.78	2.41	9.45	0.32	31	19	28	4.3
482	139.35935	45.97174	0.02574	9.45	7.89	2.80	8.49	0.20	6	14	28	22.2
483	139.55919	45.65171	0.02690	10.70	8.47	2.87	10.16	0.30	68	35	61	5.0
517	139.90499	32.35320	0.02652	9.72	8.54	2.01	9.25	0.23	24	18	45	11.3
563	141.20293	49.39827	0.02723	9.73	8.27	3.30	8.72	0.24	15	10	19	-
773	153.03446	46.29371	0.02425	10.34	8.48	2.63	10.03	0.40	47	34	66	-
776	152.84976	45.73539	0.02375	8.69	7.20	1.60	8.88	0.23	19	12	21	-
840	153.80716	56.60331	0.02667	8.82	7.43	1.24	9.41	0.07	28	17	33	8.9
889	154.25328	55.88005	0.02437	9.77	8.28	2.34	9.56	0.28	36	18	33	6.7
941	153.81151	58.69174	0.02295	8.61	7.73	1.80	9.12	0.29	6	29	49	4.5
983	162.50634	36.25677	0.02190	9.75	8.09	3.12	8.47	0.09	6	17	27	-
997	162.75426	36.19258	0.02380	9.85	7.80	2.23	9.98	0.23	55	23	47	-
999	162.49449	36.41499	0.02327	9.50	8.20	3.34	8.78	0.08	17	13	24	5.7
1020	166.86889	35.46365	0.02828	-	-	3.05	9.87	0.10	37	26	58	-
1022	166.95902	35.40299	0.02840	10.47	8.81	3.49	9.56	0.07	36	18	32	18.0
1024	166.95821	35.68483	0.02846	10.30	9.10	2.97	9.62	0.22	41	25	42	9.1
1027	167.10516	35.33068	0.02888	8.96	7.33	3.81	8.94	0.16	18	13	25	-
1042	168.52972	34.30886	0.02526	8.70	6.97	1.91	9.09	0.16	25	18	31	17.1
1104	177.57556	35.25409	0.02128	10.22	8.97	2.84	10.08	0.36	68	35	76	-
1143	185.61022	40.76168	0.02292	8.40	7.68	-0.14	9.14	0.17	28	16	27	16.9
1183	193.23760	51.82684	0.02762	8.58	7.78	1.50	8.90	0.20	16	11	22	23.2
1230	196.76312	57.86514	0.02874	8.77	7.04	2.04	9.09	0.27	19	12	22	4.6
1254	198.42330	47.29923	0.02808	8.80	7.20	1.22	9.19	0.20	23	15	25	6.3
1259	198.26018	47.34518	0.02841	8.76	7.28	1.79	9.02	0.11	17	14	30	10.4
1261	197.86026	47.44052	0.02861	9.03	7.29	2.46	8.92	0.25	15	9	15	-
1296	198.84572	35.17351	0.02309	8.90	8.12	1.82	8.98	0.19	19	12	22	7.1
1298	198.67004	35.03638	0.02374	8.67	7.46	1.61	9.21	0.28	22	14	29	13.2
1323	203.28755	40.85307	0.02400	8.88	7.70	1.24	8.97	0.33	10	22	33	3.7
1407	212.50986	38.70812	0.02576	9.86	8.31	3.81	9.67	0.21	34	28	52	-
1410	212.67758	38.71842	0.02561	8.57	7.42	1.30	9.26	0.18	23	19	47	-
1411	212.62710	38.73950	0.02606	8.95	7.86	1.23	9.44	0.15	29	16	31	12.5
1414	212.69582	38.75970	0.02570	8.74	7.46	1.72	8.81	0.14	15	11	25	-
1415	212.72923	38.78592	0.02580	8.43	7.14	1.54	9.13	0.13	14	15	31	7.2
1533	241.43411	36.27508	0.03123	9.40	7.50	1.74	9.79	0.30	44	23	38	-
1554	242.24289	36.61088	0.03014	11.02	8.83	3.33	10.42	0.31	26	50	104	26.6
1605	246.16476	41.01995	0.02712	8.79	7.33	0.66	9.70	0.10	33	15	31	6.1
1632	246.06271	41.11062	0.02926	9.97	8.21	3.27	9.70	0.22	38	17	33	9.6
1639	246.70860	40.91786	0.02915	8.93	7.68	1.83	9.21	0.34	21	29	33	9.0
1643	246.13086	40.68445	0.02943	8.80	7.49	1.10	9.06	0.28	20	18	36	-
1647	246.08427	40.86501	0.03000	9.34	7.50	2.46	9.13	0.16	17	12	44	-
1648	245.99846	41.13817	0.03029	9.08	7.39	1.34	9.59	0.27	34	17	33	20.6
1663	250.62296	42.26285	0.02750	8.78	7.27	1.27	9.08	0.14	20	16	32	15.6
1669	250.56263	42.05996	0.02780	8.82	7.68	1.96	9.17	0.22	20	18	50	19.7
1700	251.48897	39.98583	0.03020	10.17	8.22	3.18	9.69	0.36	5	20	35	7.2
1713	251.87396	40.56570	0.03108	8.92	7.44	1.39	9.68	0.32	37	19	32	-
1725	258.80617	30.45146	0.02864	9.98	8.17	2.56	9.66	0.31	39	20	34	-
1774	259.68221	58.13513	0.02908	10.95	8.85	3.60	9.98	0.39	55	26	48	13.5
1795	258.77994	58.24045	0.03101	10.20	8.35	3.08	9.78	0.26	40	18	38	-
1907	262.17343	57.11476	0.02812	-	-	-0.42	9.03	0.03	17	11	23	16.7

Table 1. Properties of additional galaxies extracted in the data cubes of the Bluedisk project. The detailed information of the targeted galaxies is presented in Paper I. From left to right, columns represent galaxy ID, Right Ascension, Declination, redshift, base-10 logarithm of the stellar mass, base-10 logarithm of the stellar surface density, NUV-r color, base-10 logarithm of the HI mass, distance to the central of the data cube (in degree), $R1$, $R_{50,\text{HI}}$, $R_{90,\text{HI}}$ and exponentially scale length rs , respectively.

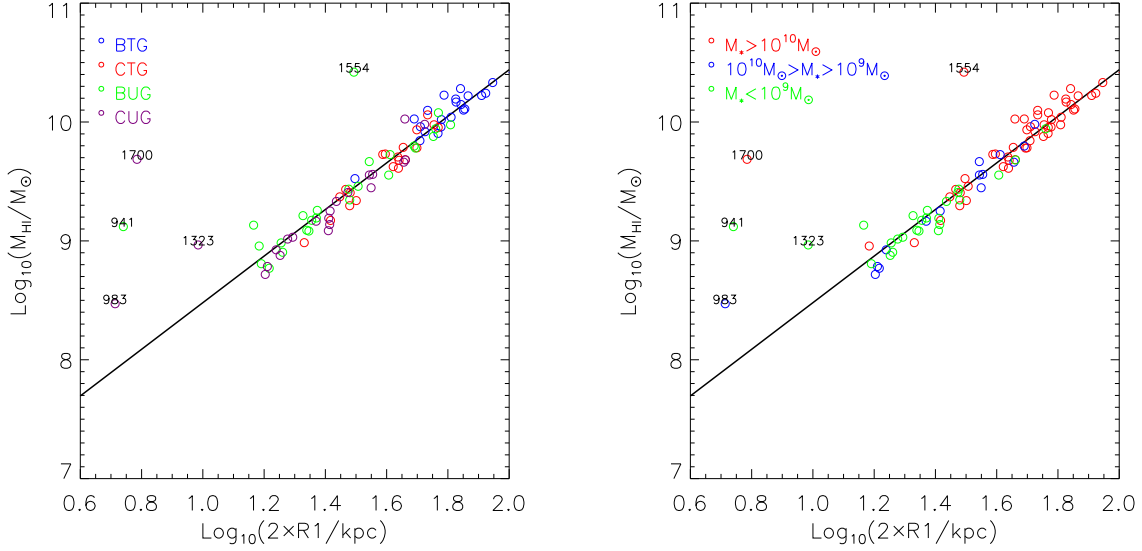


Figure 5. The HI mass-size relation for our sample. The left panel shows the mass-size relation for BTG (blue), CTG (red), BUG (green) and CUG (purple). The right panel is similar to left one but for different stellar mass ranges. Some outliers in HI mass-size relation are marked by their IDs (these galaxies are discussed in detail in section 5).

4.1 HI mass-size relation

The tight relation between the diameter of the HI disk and the total HI mass in galaxies was investigated by Broeils & Rhee (1997). Later, it was found that this relation changes very little for different kinds of galaxies (Swaters et al. 2002; Noordermeer et al. 2005). Fig. 5 shows the HI mass-size relation for our sample. The left panel shows this relation for the four subsamples: BTG (blue), CTG (red), BUG (green) and CUG (purple). The black line is from Broeils & Rhee (1997). The right panel shows the same relation for different stellar mass ranges. Some outliers far from this relation are marked by their IDs.

Almost all the galaxies closely obey this relation, which is consistent with the result of Paper I. This relation is similarly tight for galaxies with both high and low stellar masses: the average column density of HI is about same for all spiral galaxies. Wang et al. (2014) suggest that this relation is primarily a result of atomic-to-molecular gas conversion in the inner disk and is further enhanced by a homogeneous radial distribution of HI density in the outer disk of galaxies. We will investigate the nature of the handful of outliers later in the paper.

4.2 HI-optical scaling relations

In Fig. 6, we plot the HI-to-stellar mass ratio as a function of stellar mass, stellar surface mass density and NUV-r color for our sample. The HI mass fraction correlates with stellar mass, surface mass density and NUV-r, and extends the mean relations quantified for normal galaxies with stellar masses greater than $10^{10} M_{\odot}$ in former studies (Catinella et al. 2010; Cortese et al. 2011; Huang et al. 2012). We do not see different HI scaling relations for galaxies in the data cubes with a central targeted HI excess galaxy and data cubes with a central targeted control galaxy.

We plot the HI plane linking HI-to-stellar mass ratio with stellar surface mass density and NUV-r colour defined by Catinella et al. (2010) in the left panel of Fig. 7. The gray data points represent galaxies from GASS (Catinella et al. 2010). In this projection, both targeted and untargeted galaxies lie close to the HI plane. Differences arise when we focus on the *displacement* from the plane. As already found in Paper I, we observe a tilt of our observed galaxies with respect to the diagonal of the plot. The plane underpredicts the HI content of all observed galaxies at the high-HI-fraction end and slightly over-predicts it at the low-HI-fraction end of our sample. The underprediction at the high-HI-fraction end is discussed in detail by Li et al. (2012), who argue that the addition of additional parameters yield a more unbiased prediction of HI content.

The right panel of Fig. 7 shows the distributions of the deviations from the HI-plane (the black line in Fig. 7). We find a significant difference between the distributions of the galaxies in the cubes of the HI-rich targets and the galaxies in the control cubes. We perform a Kolmogorov-Smirnov (K-S) test to quantify this significance, and obtain a probability of 0.041, suggesting a 96% significance for the null hypothesis of the two samples being drawn from the same parent distribution to be rejected. It appears that on average, galaxies in the data cubes with an HI excess targeted galaxy do on average contain more HI (relative to their surface mass density and colour) than galaxies in the cubes containing a control galaxy. This suggests that galaxies associated with blue targeted galaxies are also likely to be gas-rich. This supports the observation pointed out by Kauffmann, Li & Heckman (2010), see also Weinmann et al. (2006), who found that there is more photometrically estimated HI in satellites around more star-forming primary galaxies than in satellites around less star-forming primary galaxies. In the following, we refer to this as “HI conformity”. Those authors argued

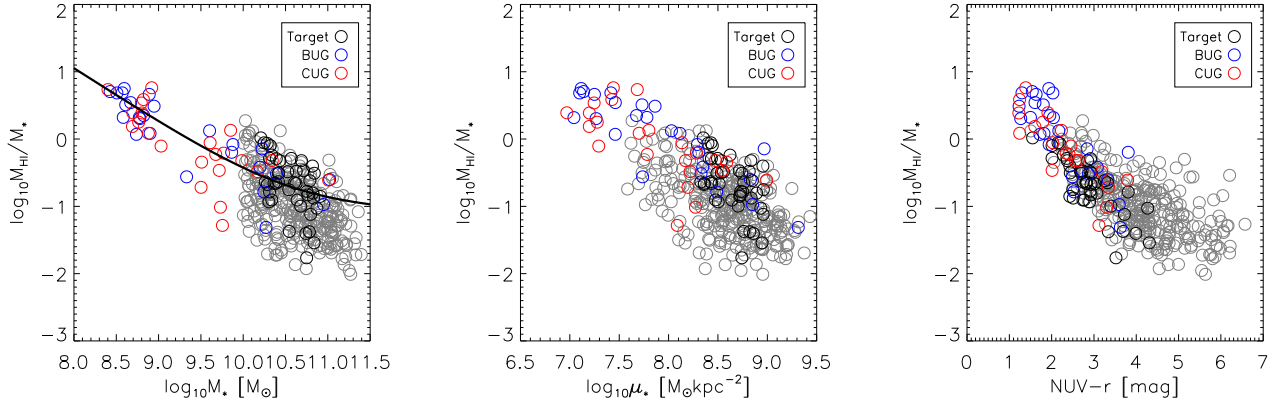


Figure 6. The HI mass fraction plotted as a function of stellar mass, stellar surface mass density and NUV-r for target galaxies (black), other galaxies in the HI-rich cubes (blue), other galaxies in the control cubes (red) and GASS sample galaxies (gray). The black curve in the left panel shows the empirical relation of HI mass fraction as a function of stellar mass, which is taken from Evoli et al. (2011).

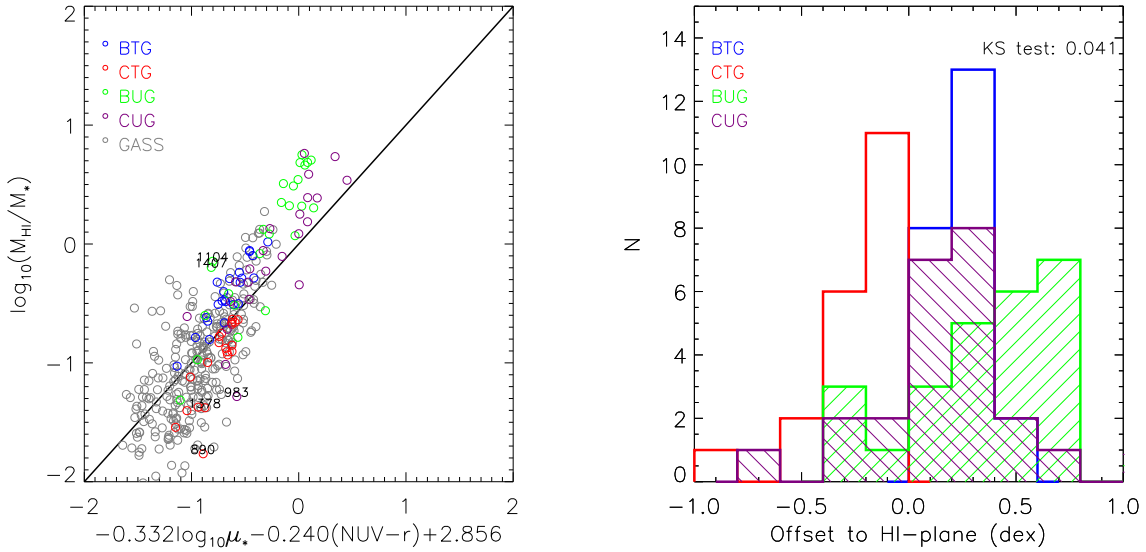


Figure 7. Left panel: HI-plane for our sample. This panel illustrates that the ratio of HI mass to stellar mass versus the combination of surface mass density and NUV-r. Galaxies in the BTG (blue), CTG (red), BUT (green), CUG (purple) samples are colour-coded. The gray data points show the GASS sample. Right panel: The distribution of deviations from the HI-plane (corresponding to the black line in the left panel) for our sample. The blue, red, green and purple distributions represent for the distributions of BTG, CTG, BUG and CUG galaxies, respectively. The K-S test probability for the difference in deviation from the HI-plane between the BUG and CUG samples is denoted at the top-right corner of the right panel.

that the satellites trace a large-scale gas reservoir that is accreted onto the central galaxies.

Next, we repeat the morphological analysis of Paper I for the additional galaxies detected in the cubes. In Fig. 8, we plot distributions of ΔCenter , $R_{90,\text{HI}}/R_{50,\text{HI}}$, rs and $rs/R1$. ΔCenter is calculated as the distance between the HI center and the r-band center, normalized by the semi-major axis of the HI ellipse. $R_{90,\text{HI}}/R_{50,\text{HI}}$ describes the concentration/extension of the HI disks. rs is the exponentially scale length of HI disks.

The galaxies in the HI-rich cubes do not differ from those in the control cubes in their distribution of ΔCenter . However, their distributions of $R_{90,\text{HI}}/R_{50,\text{HI}}$ do show a sig-

nificant difference. Galaxies in the HI-rich cubes tend to have larger $R_{90,\text{HI}}/R_{50,\text{HI}}$ than in the control cubes. If we investigate galaxies with $R_{90,\text{HI}}/R_{50,\text{HI}}$ greater than 2.0, we find almost all of them have more HI gas than the predicted by their optical properties. The distribution of the deviations from the HI-plane for these galaxies is shown in Fig. 9. The median value of the deviations is 0.44 dex, which means these galaxies have 2.7 times HI of the predicted values in general. We also find their HI to extend far beyond the optical disk. The rs and $rs/R1$ distributions of the galaxies in the HI-rich cubes do not differ significantly from those for galaxies in the control cubes.

To assess whether the density of the environment may

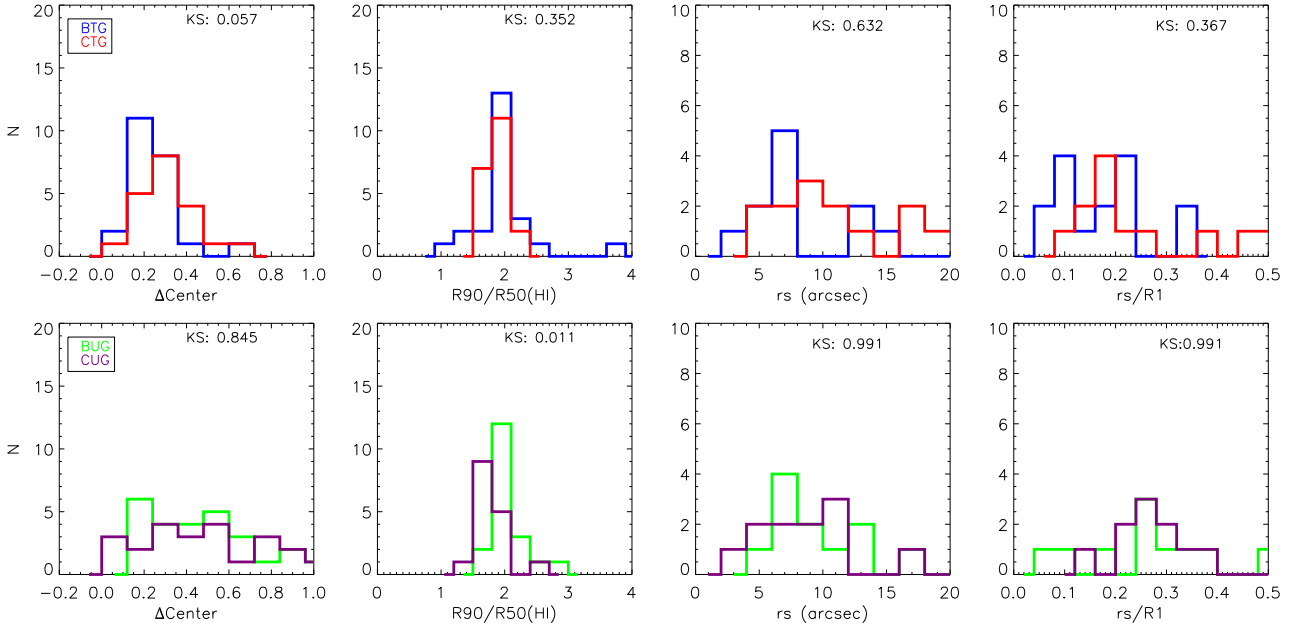


Figure 8. The distributions of Δcenter , $R_{90,\text{HI}}/R_{50,\text{HI}}$, r_s and r_s/R_1 for BTG (blue), CTG (red), BUG (green) and CUG (purple). The K-S test probability that the HI-rich and control cube distributions are drawn from the same underlying distribution is given in the top right corner of each panel.

play a role in these differences, we checked the number of SDSS spectroscopically observed galaxies of which fall in our cubes, but which have no HI detections. There are 95 galaxies with no HI detections in the HI-rich cubes and 295 galaxies with no HI detections in the control cubes. Most of these galaxies have stellar masses in the range between $10^8 M_\odot$ and $10^{10} M_\odot$. We also quantify the environment by using the 3-d reconstructed matter overdensity based on SDSS DR7 data set (Jasche et al. 2010), which is defined as $\delta = (\rho - \bar{\rho})/\bar{\rho}$, where ρ is the matter density and $\bar{\rho}$ is the mean matter density. Thus the mean overdensity of galaxies in control cubes is 10.7, while the mean over-density of galaxies in blue cubes is 4.6. It is clear that the control cubes are located in denser regions than the HI-rich cubes, and the fraction of optically-identified galaxies that have detectable HI masses is much higher in the blue cubes than in the control cubes. This may indicate that HI conformity is closely related to the environment of the galaxy.

5 MORPHOLOGY OF OUTLIERS

Galaxies accrete cold gas directly from the intergalactic medium or through interaction with companions, and lose their gas through tidal or ram pressure stripping. Some authors have tried to connect specific HI structures in galaxies with ongoing cold gas accretion, such as the existence of extra-planar gas and warped structures of HI distribution in galaxies (Wakker et al. 2007; Thilker et al. 2007; Oosterloo et al. 2010). Ram pressure stripping, especially in clusters also affect the morphology of HI disks (McConnachie et al. 2007; Bernard et al. 2012; Serra et al. 2013; Zhang et al. 2013). In this section, we investigate the structures of those galaxies which are outliers in the HI mass-size relation (see

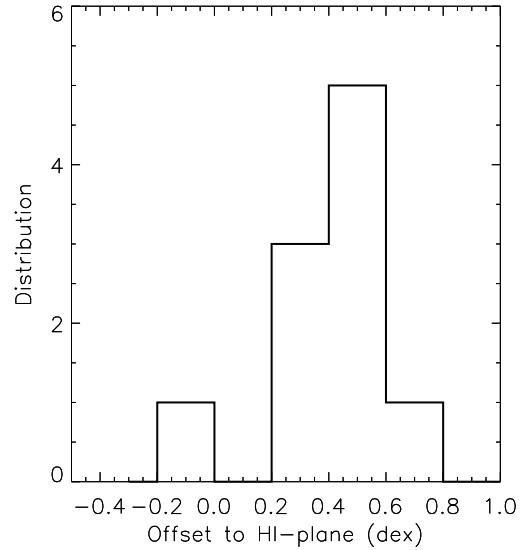


Figure 9. The distribution of deviations from the HI-plane for untargeted galaxies with $R_{90,\text{HI}}/R_{50,\text{HI}}$ greater than 2.0. The median value of these deviations is 0.44 dex.

Fig. 5) or the HI-plane (see Fig. 7). We argue that (after close inspection) either offset is an indication for ongoing interaction with the environment.

Outliers are defined to include galaxies that are offset in their HI mass by more than 0.4 dex from the normal HI mass-size relation or offset more than 0.5 dex from the HI-plane. Here we just discuss the outliers with $M_* > M_{\text{HI}}$, since the HI plane would underestimate the HI fraction for

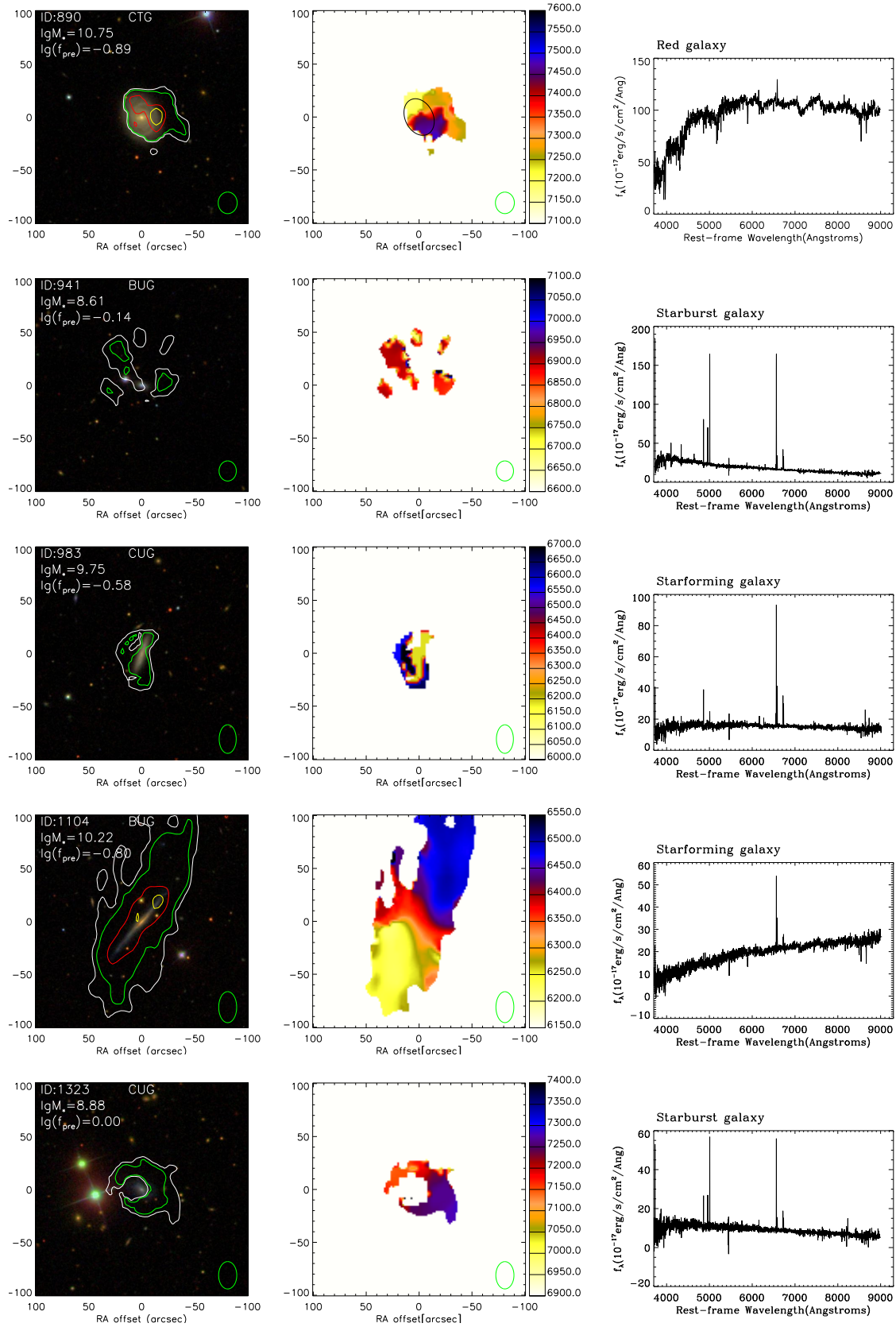


Figure 10. HI column density contours overlaid on optical images; HI velocity maps and SDSS spectra for outliers. The galaxy ID, stellar mass and the predicted HI mass fraction are labeled in the top-left-hand corner of each left panel. The white, green, red and yellow HI contours represent 2.0, 4.0, 14.0 and 20.0 times the median SNR of the outermost contour, respectively. The shape of the beam is plotted in green at the bottom-right corner of each map. All the maps are displayed as north up and east left.

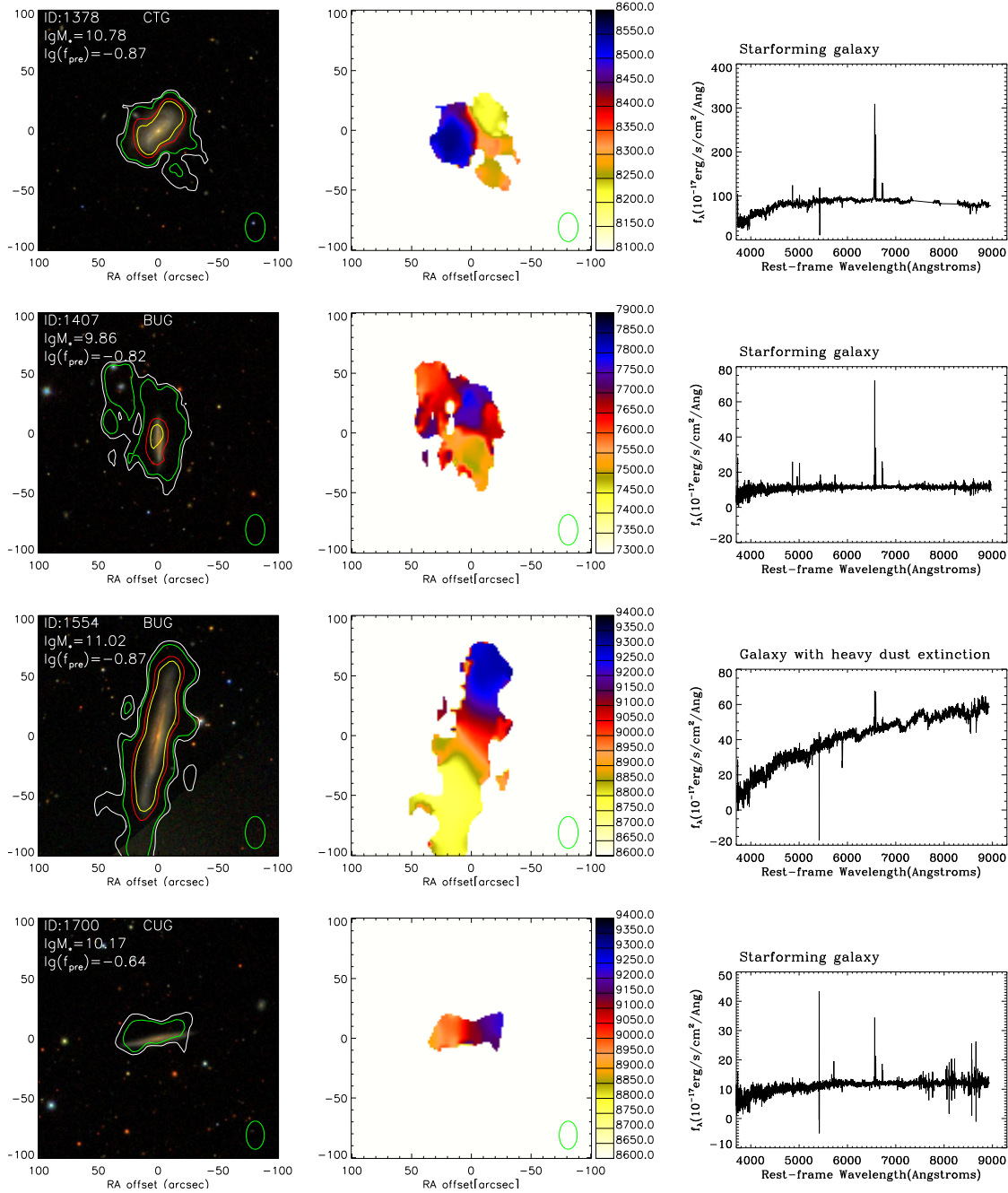


Figure 10. Continued

galaxies with $\log_{10}(M_*/M_{\text{HI}}) > 0$. We select the outliers from all cubes with “peculiar cubes” (Section 3) excluded. Note that there is no indication that outliers tend to fall preferentially into either group of galaxies around HI-rich galaxies (blue sample) or control galaxies. In table 2, we list the environment of galaxies, host system Dark Matter (DM) mass, offset from the HI mass-size relation, offset from the HI-plane, ΔCenter and $R_{90,\text{HI}}/R_{50,\text{HI}}$. The environment of galaxies (isolated or in group) and the host halo mass estimates are from Yang et al. (2007). Fig. 10 shows HI total intensity contours overlaid on an SDSS colour image, an HI velocity field and an SDSS spectrum for each of these out-

liers. The white, green, red and yellow HI contours represent 2.0, 4.0, 14.0 and 20.0 times the median SNR of the outermost HI contour, respectively. The velocity fields are derived from a Gauss-Hermite fitting procedure (den Heijer et al., in preparation).

5.1 Outliers in the HI mass-size relation

Galaxies marked 941, 1323, 1554 and 1700 are outliers from the HI mass-size relation. Galaxy 1554 and 1700 are edge-on galaxies, while Galaxy 941, 1323 and 1622 are not. We will discuss Galaxy 941, 1323, 1554 and 1700 in detail. Galaxy

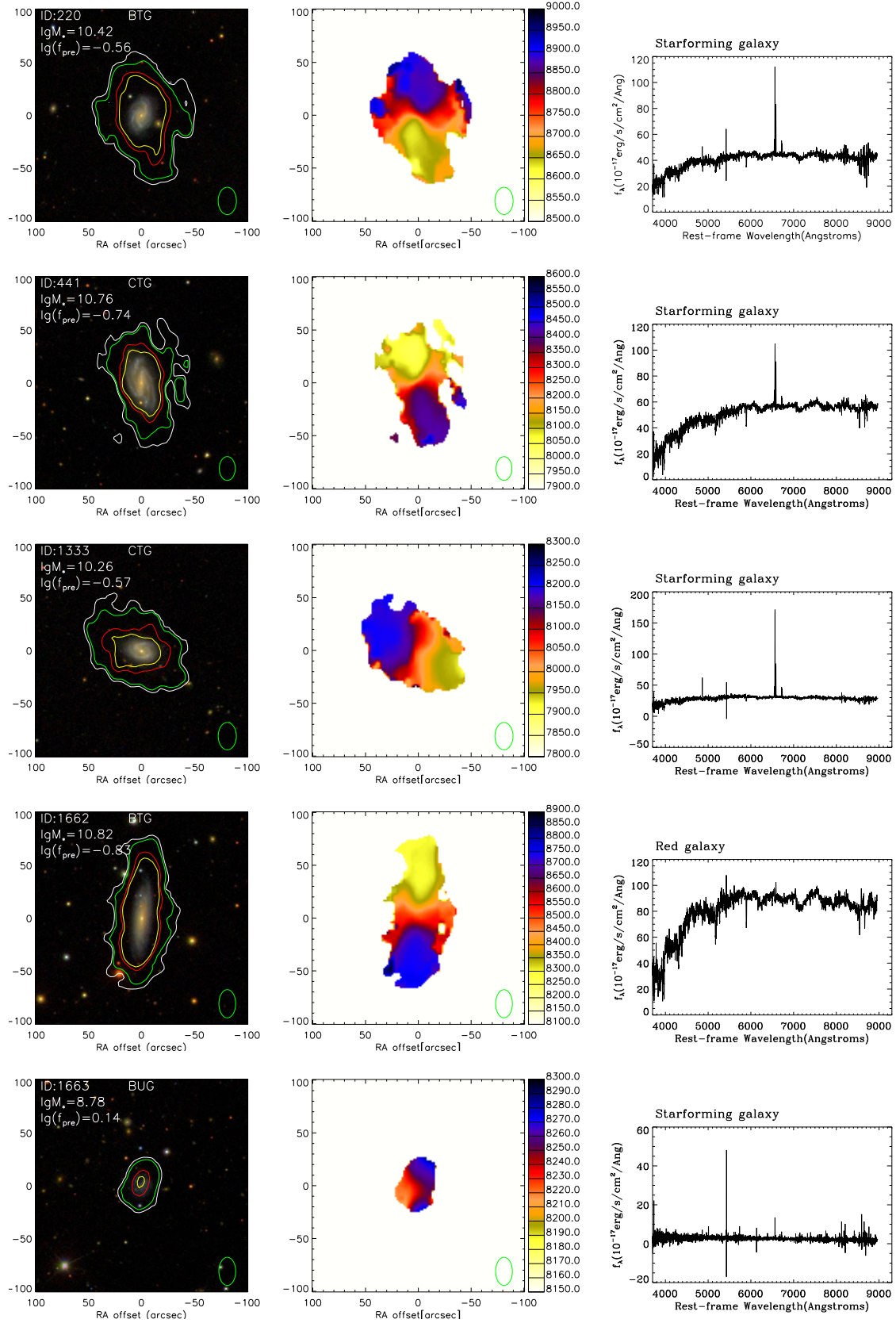


Figure 11. The same as Fig. 10 but for some of the non-outlier galaxies, selected randomly from our sample galaxies with the offset to HI mass-size relation less than 0.2 dex and the offset to HI-plane less than 0.2 dex.

ID	Environment	$\log_{10} M_{\text{halo}}$ M_{\odot}	HI MS dex	HI-plane dex	ΔCenter	$R_{90,\text{HI}}/R_{50,\text{HI}}$
941	isolated	-	1.15	0.65	0.252	1.68
1323	-	-	0.51	0.08	0.3981	1.51
1554	isolated	12.59	0.97	0.27	0.350	2.09
1700	isolated	-	1.63	0.15	0.960	1.73
890	isolated	12.37	-0.14	-0.87	0.447	1.85
983	isolated	-	0.55	-0.70	0.517	1.52
1104	isolated	-	0.09	0.66	0.129	2.16
1378	isolated	12.37	-0.02	-0.50	0.320	1.76
1407	-	-	0.12	0.62	0.517	1.87

Table 2. The list of outliers of HI mass-size relation and HI-plane. From left to right, columns represent galaxy ID, environment, halo mass, offset from normal HI mass-size relation, offset from normal HI-plane, ΔCenter and $R_{90,\text{HI}}/R_{50,\text{HI}}$, respectively.

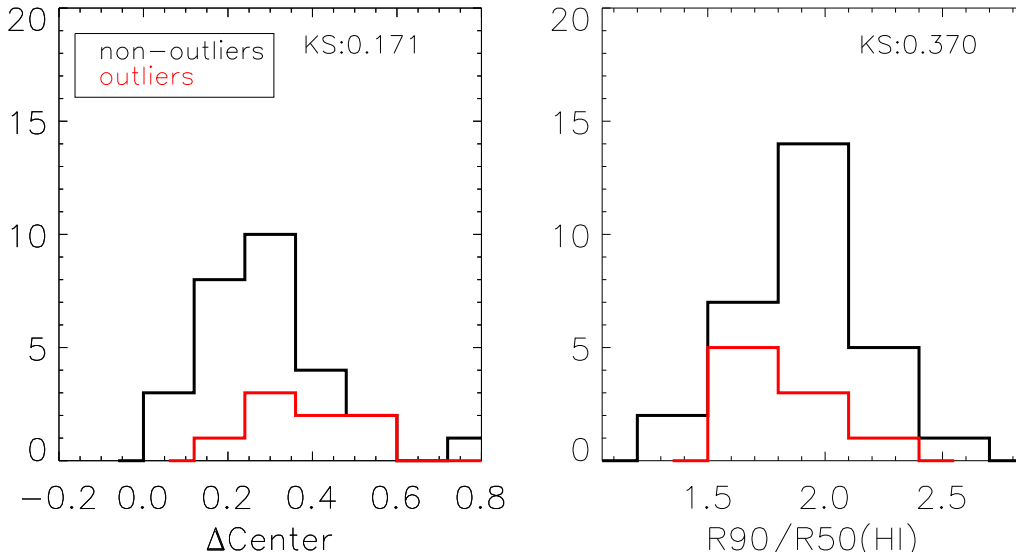


Figure 12. The distributions of ΔCenter and $R_{90,\text{HI}}/R_{50,\text{HI}}$ for outliers (red) and non-outliers (black). The K-S test probability is given in the top right corner of each panel. The non-outliers are selected from all the galaxies with both the offset to HI mass-size relation and the offset to HI-plane less than 0.2 dex.

983 is investigated in next subsection because it is also offset from the HI fundamental plane.

Galaxy 941 and 1323 are both starburst dwarf galaxies, but most of their HI is distributed asymmetrically, and is also offset from the optical disks. The HI of Galaxy 941 is distributed in patches that extend 10 times further than the optical disks. The nearby object seen in the SDSS image, is found to be a foreground star. The HI disk of Galaxy 1323 shows a big void in the region of the optical disk. There are two possible explanations for these disturbed morphologies. One is feedback processes (by AGN or by superwinds powered by SNe and stellar winds in the starburst) that push gas from inside the galaxy to the outside. The other explanation is that the HI gas in the stellar disk regions have been converted to molecular gas to sustain the fast star formation, while the HI gas in the outer regions has not had enough time to flow into the stellar disk. The stellar masses of the galaxies and their position on the “Baldwin, Phillips & Terlevich” (BPT) diagram suggests that they do not have

AGNs in their cores. We check the star formation time scale for these two galaxies. It would take more than 0.4 Gyr to consume ten percent of their total HI gas with the current star formation rate. We conclude that SNe explosions and stellar winds are the most likely cause for the holes in the HI intensity maps. In similar case, Mühle et al. (2005) argued that a huge hole in HI distribution of NGC 1569 is probably driven from SNe feedback in the center of the galaxy over the past 20Myr.

Galaxy 1554 and 1700 are edge-on galaxies. As can be seen from the SDSS spectrum, the dust extinction is very high in Galaxy 1554. The HI gas is concentrated and distributed in the stellar disk. Galaxy 1700 is a star-forming galaxy in which the HI seems to be vertically offset with respect to the stellar disk. The inclination correction creates significant uncertainty when calculating HI sizes for edge-on galaxies, since the HI disks are usually thicker than stellar disks. This may result in the offset in the HI mass-size relation.

5.2 Outliers from the HI-plane

Galaxy 983 exhibits a large offset from both the HI mass-size relation and the HI-plane. While it appears to be HI deficient with respect to the plane, its HI is more concentrated than predicted by the HI mass-size relation. In addition, a significant part of its HI appears to show irregular kinematics and is offset from the galaxy disk. Hence, morphology and kinematics suggest recent tidal or ram-pressure stripping to have removed gas in the outskirts of the galaxy.

Galaxy 890 has its HI gas compressed against the stellar disk on one side and extended to larger radius on the opposite side. Its morphological HI and optical centers are distinctly offset from each other. This is very similar to the ram-pressure stripped galaxies observed in clusters (Vollmer et al. 2004; Koopmann & Kenney 2004; Crowl et al. 2005; Chung et al. 2009). The observed HI gas mass is just 12% of the predicted value. The velocity map shows a nice spider diagram in the optical region, marked in black ellipse (see Fig. 10). For the west extended part, which also contains most of the HI, it shows a clear decrease in velocity from the inner region to the outer region. So it is likely that the direction of ram-pressure stripping is from east to west and from far to near.

Galaxy 1104 and Galaxy 1407 have at least 3 times more HI than predicted (see Fig. 7). Galaxy 1104 is a warped edge-on galaxy with a high warp amplitude. The HI distribution is also rather asymmetric, suggesting a recent interaction. Galaxy 1407 is a star-forming galaxy with a large amount of HI offset from the regularly rotating disk. It seems to be interacting with two close companions.

Galaxy 1378 has less HI gas than predicted and its HI gas is highly lopsided. It is an isolated galaxy with strong on-going star formation at the center. This galaxy possesses a large amount of gas outside the regularly rotating disk, suggesting ram-pressure stripping or tidal stripping of HI from the galaxy.

For comparison, we also present a set of “non-outlier” galaxies in Fig. 11. These are selected randomly from our sample galaxies with both the offset to HI mass-size relation and the offset to HI-plane less than 0.2 dex. Generally speaking, the HI shapes of these non-outliers are more regular compared to the HI shapes of outliers. Most of them are less asymmetric and have less HI-gas clouds in their outer region, which suggests no violent interaction with IGM. The comparison between Fig. 10 and Fig. 11 confirms that most of the outliers really have very irregular HI morphologies.

Fig. 12 compares ΔCenter (left panel) and $R_{90,\text{HI}}/R_{50,\text{HI}}$ (right panel) between outliers and non-outliers. Note that the non-outlier sample includes all the non-outliers defined in the same way as above, not only those shown in Fig. 11. The outliers appear to have larger ΔCenter and smaller $R_{90,\text{HI}}/R_{50,\text{HI}}$ when compared to the non-outliers. This result is consistent with the conclusion above, which are drawn from the example HI maps in Fig. 11. However, given the small sample size and the resulting poor statistics indicated by the K-S tests (see the K-S probabilities quoted in the figure), this result should not be overemphasized. We list ΔCenter and $R_{90,\text{HI}}/R_{50,\text{HI}}$ for the outliers in table 2. Galaxy 1700 has very large ΔCenter (~ 0.9) that is consistent with its clearly biased HI distribution. Galaxy 1407 and Galaxy 983 have relatively large

ΔCenter (~ 0.5), which are attributed to their extra-planar gas. Galaxy 1104, Galaxy 1554 and Galaxy 1407 have the largest $R_{90,\text{HI}}/R_{50,\text{HI}}$ among others. Their location on HI-plane are all above the mean relation. This is consistent with what we find in Fig. 9. However, we don’t compare rs and $rs/R1$ for the outliers, as their rs cannot be well determined.

6 SUMMARY AND DISCUSSION

In this paper, we present a catalogue of galaxies from the Bluedisk HI galaxy survey that includes sources within the cubes that were not specifically targeted for observation. These galaxies are nevertheless very interesting, because they probe the environments of unusually HI-rich galaxies, as well as a control sample of galaxies with similar masses and structural properties, but with more normal HI content.

We present the distribution of HI morphological parameters, the HI mass-size relation and scaling relations between HI gas mass fraction and galaxy mass, structure and colour. The main results in this work are listed below.

- Our sample follows established HI scaling relations as function of stellar mass, stellar surface density and colour very well, and fits the HI mass-size relation, except for a few outliers.
- Galaxies in the HI-rich cubes are displaced to higher HI gas mass fractions than predicted by the optical properties, compared to galaxies in the control cubes.
- We inspect the HI intensity maps and velocity fields of the outliers from the HI mass-size relation and the plane. We find that all these galaxies are likely to have undergone recent interaction with their environment.

The phenomenon of galactic conformity was first discovered by Weinmann et al. (2006), who argued that the properties of satellite galaxies are strongly correlated with those of their central galaxies. In particular, early-type central galaxies have a larger fraction of early-type satellites than late-type central galaxies with the same stellar mass. Subsequently, Kauffmann, Li & Heckman (2010) found that the total mass of gas in satellites has a strong correlation with the colours and specific star formation rates of central galaxies of all stellar masses, and that this correlation extends out to radii of 1 Mpc or more. This suggests that more gas-rich galaxies should have more gas in satellites in their immediate surroundings. This work was, however, based on optical proxies for HI content and not on real HI data. In this paper, we find that galaxies in the large-scale environment of HI-rich targeted galaxies tend to be HI-rich and to have a larger $R_{90,\text{HI}}/R_{50,\text{HI}}$. Our findings thus support the conjectures presented in (Kauffmann, Li & Heckman 2010).

Weinmann et al. (2006) and Ann, Park & Choi (2008) argued that the X-ray-emitting hot gas of host early-type central galaxies can deprive their satellites of their gas reservoirs through hydrodynamic interactions. However, this cannot explain the conformity effect in low mass halos. Kauffmann, Li & Heckman (2010) argued that satellite galaxies trace the high density peaks of underlying reservoir of ionized gas, which provides fuel for star formation in central galaxies.

In this work we have been able to study a few galaxies

which have irregular HI shapes and anomalous HI gas content. In most cases, we find signatures of interaction with the environment that is suggestive of tidal or ram pressure stripping, though two galaxies are found (1407 and 1104) that may be accreting HI clouds.

ACKNOWLEDGMENTS

EW and CL would like to thank the hospitality of the Max Planck Institute for Astrophysics while this work was being initiated. EW is grateful to Paolo Serra and Zhixiong Liang for helpful discussion on data analysis progress, to Milan den Heijer for providing the Gauss-Hermite velocity maps, and to Attila Popping for readily providing his primary beam attenuation model. This work is supported by National Key Basic Research Program of China (No. 2015CB857004), NSFC (Grant No. 11173045, 11233005, 11325314, 11320101002), the Strategic Priority Research Program “The Emergence of Cosmological Structures” of CAS (Grant No. XDB09000000), and the exchange program between CAS and the Max Planck Society.

Funding for the SDSS and SDSS-II has been provided by the Alfred P. Sloan Foundation, the Participating Institutions, the National Science Foundation, the U.S. Department of Energy, the National Aeronautics and Space Administration, the Japanese Monbukagakusho, the Max Planck Society, and the Higher Education Funding Council for England. The SDSS Web Site is <http://www.sdss.org/>. The SDSS is managed by the Astrophysical Research Consortium for the Participating Institutions. The Participating Institutions are the American Museum of Natural History, Astrophysical Institute Potsdam, University of Basel, University of Cambridge, Case Western Reserve University, University of Chicago, Drexel University, Fermilab, the Institute for Advanced Study, the Japan Participation Group, Johns Hopkins University, the Joint Institute for Nuclear Astrophysics, the Kavli Institute for Particle Astrophysics and Cosmology, the Korean Scientist Group, the Chinese Academy of Sciences (LAMOST), Los Alamos National Laboratory, the Max-Planck-Institute for Astronomy (MPIA), the Max-Planck-Institute for Astrophysics (MPA), New Mexico State University, Ohio State University, University of Pittsburgh, University of Portsmouth, Princeton University, the United States Naval Observatory, and the University of Washington.

REFERENCES

- Ann H. B., Park C., Choi Y.-Y., 2008, *MNRAS*, 389, 86
- Becker R. H., Helfand D. J., White R. L., Gregg M. D., Laurent-Muehlheisen S. A., 2012, *VizieR Online Data Catalog*, 8090, 0
- Becker R. H., White R. L., Helfand D. J., 1995, *ApJ*, 450, 559
- Bernard E. J., Ferguson A. M. N., Barker M. K., Irwin M. J., Jablonka P., Arimoto N., 2012, *MNRAS*, 426, 3490
- Binney J., Dehnen W., Bertelli G., 2000, *MNRAS*, 318, 658
- Boomsma R., Oosterloo T. A., Fraternali F., van der Hulst J. M., Sancisi R., 2005, *A&A*, 431, 65
- Broeils A. H., Rhee M.-H., 1997, *A&A*, 324, 877
- Calcáneo-Roldán C., Moore B., Bland-Hawthorn J., Malin D., Sadler E. M., 2000, *MNRAS*, 314, 324
- Catinella B. et al., 2010, *MNRAS*, 403, 683
- Chang J., Macciò A. V., Kang X., 2013, *MNRAS*, 431, 3533
- Chaves T. A., Irwin J. A., 2001, *ApJ*, 557, 646
- Chung A., van Gorkom J. H., Kenney J. D. P., Crowl H., Vollmer B., 2009, *AJ*, 138, 1741
- Condon J. J., Cotton W. D., Greisen E. W., Yin Q. F., Perley R. A., Taylor G. B., Broderick J. J., 1998, *AJ*, 115, 1693
- Conselice C. J., Mortlock A., Bluck A. F. L., Grützbauch R., Duncan K., 2013, *MNRAS*, 430, 1051
- Cortese L., Catinella B., Boissier S., Boselli A., Heinis S., 2011, *MNRAS*, 415, 1797
- Crowl H. H., Kenney J. D. P., van Gorkom J. H., Vollmer B., 2005, *AJ*, 130, 65
- Evoli C., Salucci P., Lapi A., Danese L., 2011, *ApJ*, 743, 45
- Huang S., Haynes M. P., Giovanelli R., Brinchmann J., 2012, *ApJ*, 756, 113
- Jasche J., Kitauro F. S., Li C., Enßlin T. A., 2010, *MNRAS*, 409, 355
- Kapferer W., Kronberger T., Ferrari C., Riser T., Schindler S., 2008, *MNRAS*, 389, 1405
- Kauffmann G., Li C., Heckman T. M., 2010, *MNRAS*, 409, 491
- Koopmann R. A., Kenney J. D. P., 2004, *ApJ*, 613, 866
- Kregel M., Sancisi R., 2001, *A&A*, 376, 59
- Li C., Kauffmann G., Fu J., Wang J., Catinella B., Fabello S., Schiminovich D., Zhang W., 2012, *MNRAS*, 424, 1471
- Mayer L., Mastropietro C., Wadsley J., Stadel J., Moore B., 2006, *MNRAS*, 369, 1021
- McCarthy I. G., Frenk C. S., Font A. S., Lacey C. G., Bower R. G., Mitchell N. L., Balogh M. L., Theuns T., 2008, *MNRAS*, 383, 593
- McConnachie A. W., Venn K. A., Irwin M. J., Young L. M., Geehan J. J., 2007, *ApJ*, 671, L33
- Moore B., Katz N., Lake G., Dressler A., Oemler A., 1996, *Nature*, 379, 613
- Moran S. M. et al., 2012, *ApJ*, 745, 66
- Mühle S., Klein U., Wilcots E. M., Hüttmeister S., 2005, *AJ*, 130, 524
- Noordermeer E., van der Hulst J. M., Sancisi R., Swaters R. A., van Albada T. S., 2005, *A&A*, 442, 137
- Oosterloo T. et al., 2010, *MNRAS*, 409, 500
- Popping A., Braun R., 2008, *A&A*, 479, 903
- Sancisi R., 1976, *A&A*, 53, 159
- Sancisi R., Fraternali F., Oosterloo T., van der Hulst T., 2008, *A&A Rev.*, 15, 189
- Sault R. J., Teuben P. J., Wright M. C. H., 1995, in *Astronomical Data Analysis Software and Systems IV*, Shaw R. A., Payne H. E., Hayes J. J. E., eds., Vol. 77, p. 433
- Serra P. et al., 2013, *MNRAS*, 428, 370
- Serra P. et al., 2012, *MNRAS*, 422, 1835
- Shang Z. et al., 1998, *ApJ*, 504, L23
- Silk J., Mamon G. A., 2012, *Research in Astronomy and Astrophysics*, 12, 917
- Swaters R. A., van Albada T. S., van der Hulst J. M., Sancisi R., 2002, *A&A*, 390, 829
- Thilker D. A. et al., 2007, *ApJS*, 173, 538
- Vollmer B., Balkowski C., Cayatte V., van Driel W., Huchtmeier W., 2004, *A&A*, 419, 35

- Wakker B. P. et al., 2007, ApJ, 670, L113
Wang J. et al., 2014, MNRAS, 441, 2159
Wang J. et al., 2013, MNRAS, 433, 270
Wang J. et al., 2011, MNRAS, 412, 1081
Weinmann S. M., van den Bosch F. C., Yang X., Mo H. J.,
2006, MNRAS, 366, 2
Yang X., Mo H. J., van den Bosch F. C., Pasquali A., Li
C., Barden M., 2007, ApJ, 671, 153
Zhang W., Li C., Kauffmann G., Xiao T., 2013, MNRAS,
429, 2191

This paper has been typeset from a \LaTeX file prepared by the author.